

Dielectric Spectroscopic investigation of Reversible Photo-induced Changes in Amorphous Ge₂Sb₂Se₅ Thin Films^{§*}

Yaw S. Obeng^{§†}, Nhan V. Nguyen, Papa K. Amoah, Jungjoon Ahn,
Physical Measurement Laboratory,
National Institute of Standards and Technology (NIST)
100 Bureau Drive, Gaithersburg, MD 20799

Mikhail Y. Shalaginov, Juejun Hu
Department of Materials Science and Engineering,
Massachusetts Institute of Technology, Cambridge, MA 02139, USA.

Kathleen A. Richardson
College of Optics and Photonics,
Department of Materials Science and Engineering,
University of Central Florida, Orlando, FL 32816, USA

Certain commercial equipment, instruments, or materials are identified in this report to specify the experimental procedure adequately. Such identification does not imply recommendation or endorsement by the National Institute of Standards and Technology, nor does it imply that the materials or equipment identified are necessarily the best available for the purpose.

**Contribution of the National Institute of Standards and Technology, not subject to copyright.*

*†*Corresponding author, email address: yaw.obeng@nist.gov

*§*ORCID: 0000-0002-4880-1689

Abstract

Broadband dielectric spectroscopy (BDS) was used to study thin films of Ge₂Sb₂Se₅ exposed to low fluence UV-irradiation that resulted in thermally reversible photo-induced changes (PICs) on the film surfaces. Changes were characterized by reversible changes in film morphology and changes in the microwave scattering signature prior to and following irradiation. The PIC resulting from irradiation formed a low modulus and electrically resistive layer at the film surface. Modest heating of the photo-exposed material to about 60 °C, anneals out the photo-formed layer to leave behind a very thin layer of smooth, thermally stable material at the film surface. Re-exposure of the material to UV-light recreated a foamy layer, which anneals away with modest heating over several cycles. The broadband microwave insertion loss (S_{21}) increased with the film morphology changes after UV light exposure and decreased with thermal anneal over several cycles. These changes are correlated with transformations in the film's surface morphology, and

possibly structural modifications in the amorphous film. Thus, the BDS analysis provided interesting new insights into the nature of photo-induced processes in chalcogenide films, such as the electrical resistance consequences of morphological / structural changes.

1.0 Introduction

Chalcogenide glasses, essentially semiconducting alloys, exhibit a wide range of photo-induced phenomena such as photo-induced darkening/bleaching, photo-fluidity, structural relaxation, expansion, and contraction [1] [2] [3]. Understanding and control of such photo-induced phenomena are technologically important for many applications, including waveguide writing, in-memory computing and information storage [4, 5], chiroptical switches [6], photonic trimming, and chiral metamaterials [7]. Such light-induced structural changes are either isotropic or anisotropic depending on the pumping light's polarization and can be partially or fully reversed by the application of external stimuli (e.g., by changing the temperature or the wavelength of the incident light). The photo-induced anisotropy below melting point can be the result of photoexcitation, electronic / electric field effects, accumulation, alignment of defects, or a combination of these effects [8] [9]. These changes are often completely reversed by annealing the materials at temperatures just under the material's glass-transition temperature, T_g . It is important to realize that the material is always in an amorphous state during the photo-induced morphological changes [10].

Mechanistically, the structural origins of the physical anisotropy (PA) can be classified into two groups: (i) a variety of relatively isolated atomic events that occur at short length scales such as the spatial redistribution of covalent bonds, directional changes in the electric dipole moment arising from defect sites, or lone-pair electron orbitals, or (ii) the orientation of structural elements that interact at longer length scales or the cooperative effect of local anisotropic events resulting in a global distortion of the amorphous network [11]. All these PA mechanisms involve changes in polarizability, be it changes in bond polarizability, the repolarization of the permanent electrical dipoles of molecules in reaction to the changing electric fields, or the distortion of the molecules in an electric field. The polarizability determines the material's dielectric response to electromagnetic radiation; in simple one-component systems, the dielectric polarization is mainly due to polarization (i.e., molecular-, atomic-, ion-space charge- and electron cloud polarization). For example, molecules have inherent dipole moments which rearrange along the electric field direction in an external EM field; the vector sum of all the dipole moments results in the molecular polarization. In electromagnetic waves, such as microwaves, the presence of an applied electric field, E , causes the dipolar moment, p , of the molecule to experience a torque, G , to orientate the dipolar moment parallel to the electric field. This instigates microwave absorption / energy dissipation during the rotation and orientation of the dipoles [12]. The dipoles oscillate to keep up with the changing external electric fields, and at some critical frequency, the polarizability cannot be maintained, resulting in dielectric loss. At high frequencies, dielectric polarizability sets the scale for radiation absorption, while at low

frequencies, it determines the nonlinear effects. Screening bound- and mobile charges set the scale for insulator-metal transitions, and mediate interactions among charge carriers and between charge carriers and phonons [13] [14].

For such material, we define a complex dielectric function that measures the electric displacement field due to the presence of an electric field in a dielectric material as written as Equation 1:

$$\varepsilon(\omega) = \varepsilon_1(\omega) + i\varepsilon_2(\omega) \quad (1)$$

where, $\omega = 2\pi c/\lambda$ is the angular frequency, c is the speed of light and λ is the wavelength.

In equation 1, $\varepsilon_1(\omega)$ describes how much the material is polarized when an electric field is applied, and $\varepsilon_2(\omega)$ is related to the photon energy absorption of the material [15] [16]. Broadband microwave dielectric spectroscopy (BDS) measures the material under test's (MUT's) complex relative permittivity (i.e., dispersive, and dissipative dielectric behavior) as a function of frequency, as illustrated by Equation 1, and characterizes materials according to their unique dielectric properties which are related to the polarizability of the chemical bonds within the analyte [17].

When microwaves (MW) interact with an analyte (i.e., here, the MUT) the probing microwave signal scatters according to the material's permittivity, with conduction loss and polarization as the two most important factors determining complex permittivity. During the signal scattering, a portion of the radiation is transmitted through the sample while the remainder is reflected toward the source. The ratio of transmitted to reflected energies (i.e., the extent of scattering) depends in part on the impedance mismatch between the MUT and the source, typically 50 Ω for most radio frequency (RF)/microwave applications. The signal scattering from the electrical interfaces is summarized as a matrix of S-parameters that quantifies how RF energy propagates through a multiport network such as a vector network analyzer (VNA). The probe microwave characteristics are convoluted with the transfer function of the waveguide loaded with the DUT, i.e., $h(f)$, to generate the output S-parameter [18]. Thus, in the referenced work, the S-parameters are functionals of frequency and external stimuli on the material (i.e., $F[h(f)]$). A typical two-port measurement contains four S-parameters (S_{11} , S_{21} , S_{12} , and S_{22}) which are vector quantities representing the magnitude and the phase of the frequency-dependent characteristics of the MUT. The S_{21} and S_{12} describe the magnitude and phase difference in degrees between a transmitted signal and an incident signal, while S_{11} and S_{22} represent the reflected signals to their ports of origin due to impedance mismatch source and the MUT. The S-parameters can be analytically transformed to produce the characteristic circuit element of the analyte by using techniques such as inverse scattering transform [19] [20]. If the chemical changes responsible for the PA /PIC are not permanent, we can use techniques such as density functional perturbation theory (DFPT) to gain predictive microscopic quantum mechanical insights into mechanisms behind the observed electrical properties [21].

Chalcogenide atoms are electron-rich and highly polarizable; hence, they readily absorb microwave energy leading to distortion as the electrons transfer from one stable state to an excited state with higher energy, forming the electron polarization, in the rapidly changing electric fields. Indeed, atomic polarization and electronic polarization are inevitable in the microwave range in chalcogenide systems. In this paper, we use broadband dielectric spectroscopy (BDS) to rapidly interrogate a dynamic range of material characteristics to elucidate the photo-induced changes (PIC) and express the changes as electrical properties. Here, we use MW insertion loss characteristics (S_{21}) to as a proxy for changes in the MUT's electrical resistance / impedance in response to applied stimuli as electrical impedance changes[22]. More rigorous analyses of the relationship between S-parameters and device (MUT) impedance are available in the open literature [23] [24].

2.0 Experimental

The $\text{Ge}_2\text{Sb}_2\text{Se}_5$ bulk glass was prepared using a standard melt quench technique from high-purity (99.999%) raw elements [25]. The film deposition was performed using a custom-designed system (PVD Products, Inc.) following previously established protocols [26]. Stoichiometries of the films were confirmed using wavelength-dispersive spectroscopy (WDS) on a JEOL JXA-8200 SuperProbe Electron Probe Microanalyzer (EPMA) to be within 2% (atomic fraction) deviation from target compositions. The “as-deposited” unannealed samples were stored in translucent polypropylene carrier cases, in a nitrogen-filled box, under laboratory ambient light for extended periods before use.

Figure 1 shows a schematic of the BDS experimental setup used in this work. The MUT was loaded onto a sensor, a ground-signal-ground (GSG) coplanar waveguide (CPW), situated in a temperature-controlled environment reactor, a 3.8 cm diameter quartz tube resistively heated with a heating tape (HTS/Amptek Standard Mono-Tapes, Stafford, Tx)[#]. The sample temperature was measured with a C-type thermocouple, inside the reactor just above the MUT. The CPW sensor was fabricated from a tin-covered printed circuit board (FR4), 61 mm long, with 5 mm wide ground lines separated from the 1.5 mm wide signal line by 1.2 mm gaps. The cables from the vector network analyzer (VNA) were connected to the CPW with edge mount connectors (Amphenol RF SMA, Amphenol RF, Danbury, CT)[#]. The cables connecting the CPW were de-embedded, with a 2-port short-open-load-through (SOLT) calibration in which the calibration standards were attached to the end of the feed cables, i.e., the reference plane of the measurement was moved from the port faces of the VNA (SPARQ™ Signal Integrity Network Analyzer, Model 4002E, Teledyne LeCroy, Chestnut Ridge, NY) [#] to the connector/cable interface. Thus, the launch connectors and CPW were part of the MUT. In this configuration, the reported S-parameters generated results from the chalcogenide thin film coated substrates perturbing the electric fields emanating from the signal and terminating on the ground lines in the CPW. Although we monitored a broadband range (0.1 GHz to 20 GHz), the reporting frequency of 0.5

GHz was chosen based on the sample dimensions, the absence of resonances, and minimized signal reflections.

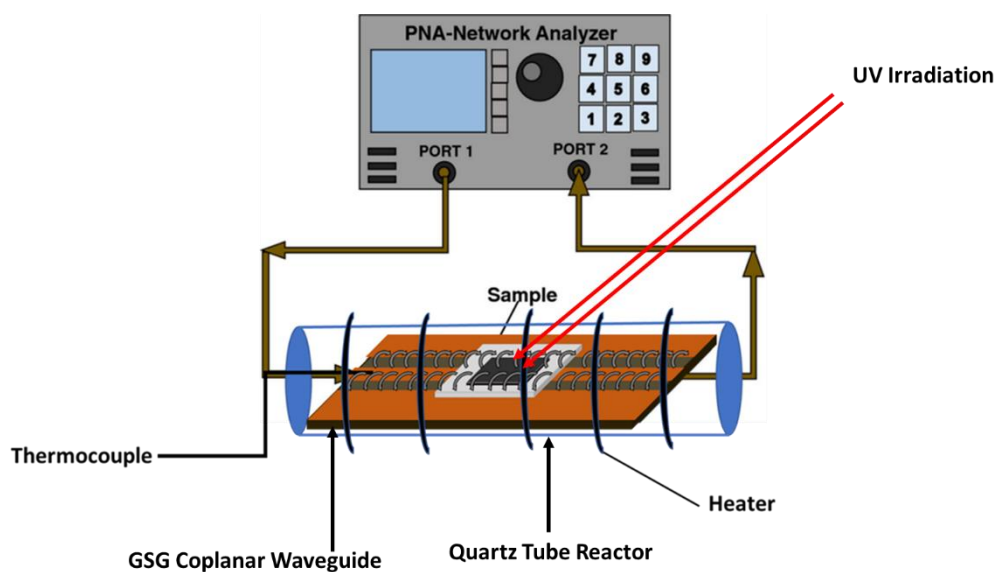


Figure 1: A schematic representation of experimental setup used in this study showing the $\text{Ge}_2\text{Sb}_2\text{Se}_5$ sample on a ground-signal-ground (GSG) waveguide situated in a controlled environment (Pyrex tube).

After initial readings, the samples were illuminated with a UV lamp (Analytik Jena 95-0016-14 Shortwave UV lamp; 4 W, 115 VAC/60 Hz, Cole-Palmer, Vernon Hills, IL)[#] and held 5 cm above the outer wall of the quartz reactor. Readings were taken every 30 seconds while being continuously irradiated, under continuous house nitrogen flow. In this work, the samples were irradiated with either UV-AB (315-400 nm, 3.94 – 3.1 eV at a fluence of $660 \mu\text{W}/\text{cm}^2$) or with UV-C (280-315 nm, 4.43 -3.90 eV at a fluence of $125 \mu\text{W}/\text{cm}^2$), measured on the outer wall of the quartz tube reactor. These wavelengths are well above the 1.2 eV bandgap of the thin films studied in this work. We expected high absorption that could induce significant warming, so experiments were conducted under constant house nitrogen flow as a coolant and inert environment. We did not analyze the films for compositional nor chemical bonding changes after the UV irradiation nor after thermal anneal.

AFM data was collected on a Bruker Dimension Icon XR platform (Bruker, Santa Barbara, CA)[#] in a “ScanAsyst” mode, with a ScanAsyst-Air-HPI cantilever and tip. ScanAsyst imaging mode is an optimization scanning mode for AFM. In this mode, the AFM continuously monitors image quality and makes the appropriate adjustments parameters such as setpoints, feedback gains, and scan rates to collect force curves at every pixel in the image. The peak force of each of the force curves

is used as the imaging feedback signal, to provide direct force control which enables it to operate at very low forces [27].

All spectroscopic ellipsometry (SE) measurementsⁱ were performed on a J. A. Woollam M2000x spectroscopic ellipsometer (J.A. Woollam Company, Lincoln, NE)[#]. The measured spectral range was scanned from 2.0 eV to 5.8 eV in steps of 0.02 eV with three angles of incidence of 65°, 70°, and 75°[28].

3.0 Results and Discussion

3.1 Microwave Monitoring Changes in Films Electrical Properties

Figure 2 shows the typical evolution of the microwave insertion loss (S_{21} amplitude at 0.5GHz) of an 820 nm thick $\text{Ge}_2\text{Sb}_2\text{Se}_5$ film on Corning glass (Pyrex 7740, Corning, Corning, NY)[#] as a function of sequentially applied experimental stimuli under constant nitrogen flow: (I) UV-A illumination at room temperature, (II) temperature ramp from room temperature to 60°C, (III) dark storage at room temperature, and (IV) UV-A illumination at room temperature. We note that the application of different stimuli resulted in different S_{21} values indicating changes in the MUT's impedance due to changes in chalcogenide thin films. The jump in S_{21} from -12.5 to -13.5 dB in region (I) represents the initial UV-A induced transformation of the 'as-received' film. The initial optical transformation occurred after a dose of 0.8 mW/cm² of UV-AB irradiation, in contrast, the subsequent UB-induced switches (e.g., region IV) were almost instantaneous. The PA responsible for the observed S_{21} appeared to be reversible. In the following, we examine the impact of each applied stimulus on S_{21} . The reduction in insertion loss between 290-300 s in Figure 2 is due to the onset of the heating cycle to reverse the photo-induced changes (PIC) in region (IV). The altered states were stable for hours, before changing upon the application of different stimuli. It is also worth noting that the changes in S_{21} are relatively small, consistent with the fact that only about 2% of the film thickness was changed by the applied stimuli.

The UV-AB light induced changes in the analytes were quantified by a change in S_{21} amplitude; the insertion loss increased as the impedance of the film increased in a stepwise manner with increasing UV fluence. The impedance increase is due to increased film low-frequency resistance which is indicative of reduced carrier concentration and / or mobility, because of PIC in the MUT. The film gets more resistive possibly due to optically induced bonding changes that alter the electric-dipole moments and their Coulombic interaction with their environments [9] [29].

The UV-radiation energy (3.15 – 4.43 eV for UV-AB, and 4.43 -12.40 eV for UV-C, respectively) far exceeds the optical band gap of the thin films. When the thin films are irradiated with the UV-light, part of the energy induces valence to conduction band transitions, and the excess energy dissipates as phonons. The interaction of the phonon and the local configuration causes charge separation, possibly in the valence alternation pairs [30] [31]. The e-h pairs (i.e., hot charge carriers) subsequently recombine non-radiatively to generate heat[32], resulting in a localized

heating to temperatures that could exceed the glass transition temperature (T_g , of 245 °C [33]) to produced localized compositional and phase changes [34].

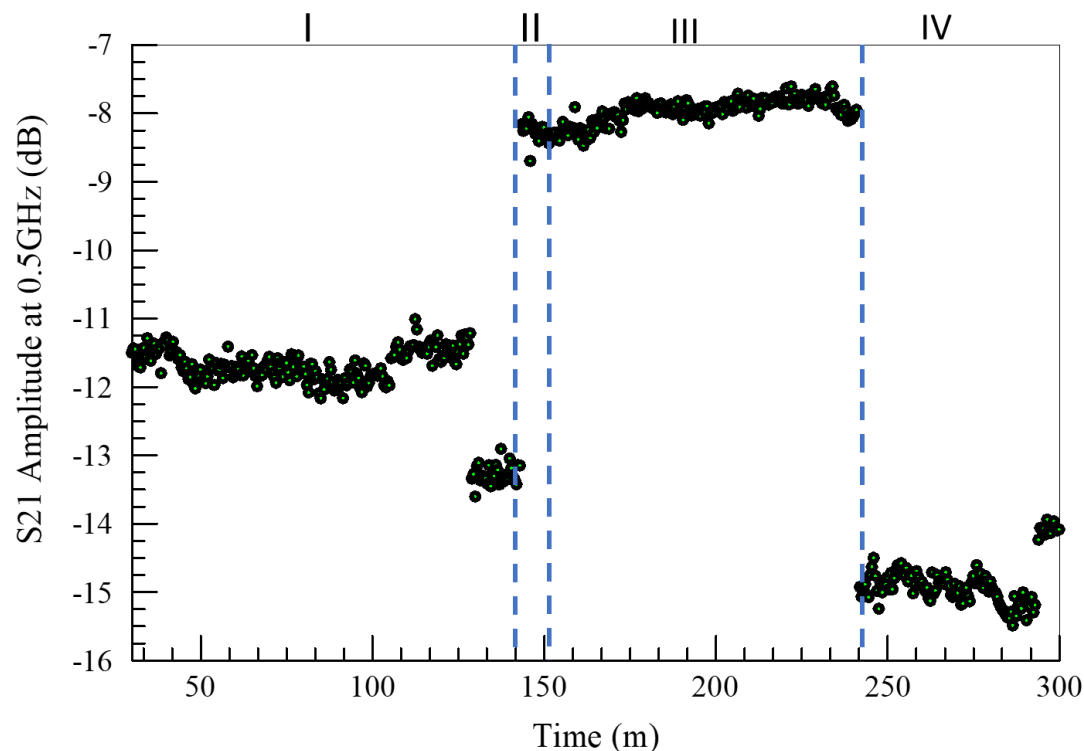


Figure 2: Typical evolution of the Microwave Insertion Loss (S21) of an 820 nm $\text{Ge}_2\text{Sb}_2\text{Se}_5$ thin film on Corning glass as function of applied experimental stress under constant nitrogen flow: (I) UV-A illumination at room temperature, (II) temperature ramp from room temperature to 60°C, (III) room temperature dark storage, and (IV) UV-A illumination at room temperature.

At the nanometer scale, these amorphous thin films are comprised of inhomogeneous unique nanoregions which could selectively undergo photo-induced changes during light absorption due to localized physicochemical processes. Specifically, the selective changes occur at those nanoregions whose maximum absorption axis coincides with the direction of polarization in the light wave [35]. Thus, the proposed phase change is random in the otherwise amorphous film and may be confined to the air/film interfaces because of the limited penetration depth of the UV-light used to set up a photo generated bilayer. As we show below, this photo generated top layers is metastable, and can partially revert to the bulk material with mild thermal anneal. Furthermore, the e-h recombination reduces the type and mobilities of defects/charges and will result in decreased film resistance, as we observed. Thermal annealing at modest temperatures reverts the charge recombination to increase the conductivity of the film, as shown in Figure 3.

Notice the incubation period before the S_{21} change during the initial UV-AB illumination (Segment I)), but not in the subsequent following the thermal anneal re-illumination (Segment IV). This could be indicative of highly cooperative light-induced transformation, which self-accelerates once points of nucleation form, in the creation of the foamy overlayer at the air interface in the as-deposited film[36]. The nuclei appear to survive the thermal anneal and the long storage at room temperature (Segment III), such that the overlayer forms spontaneously when the film is re-exposed to UV-light.

Figure 3 shows the evolution of the insertion loss with increasing reactor temperature during Segment-II of Figure 2. The figure suggests that the film resistance decreased monotonically with increasing temperature, at temperatures above 40°C, from the high resistance set by the photo-induced changes from the previous UV irradiation. As we show later, thermal exposure of the as-deposited amorphous film to temperatures around 60°C did not change the electrical, the surface morphology, nor optical properties of the analyte. Thus, the resistance change in the photo-exposed films suggests that the PIC responsible for the microwave absorption can be reversed with thermal heating. We did not exceed 60°C because of experimental setup limitations [37].

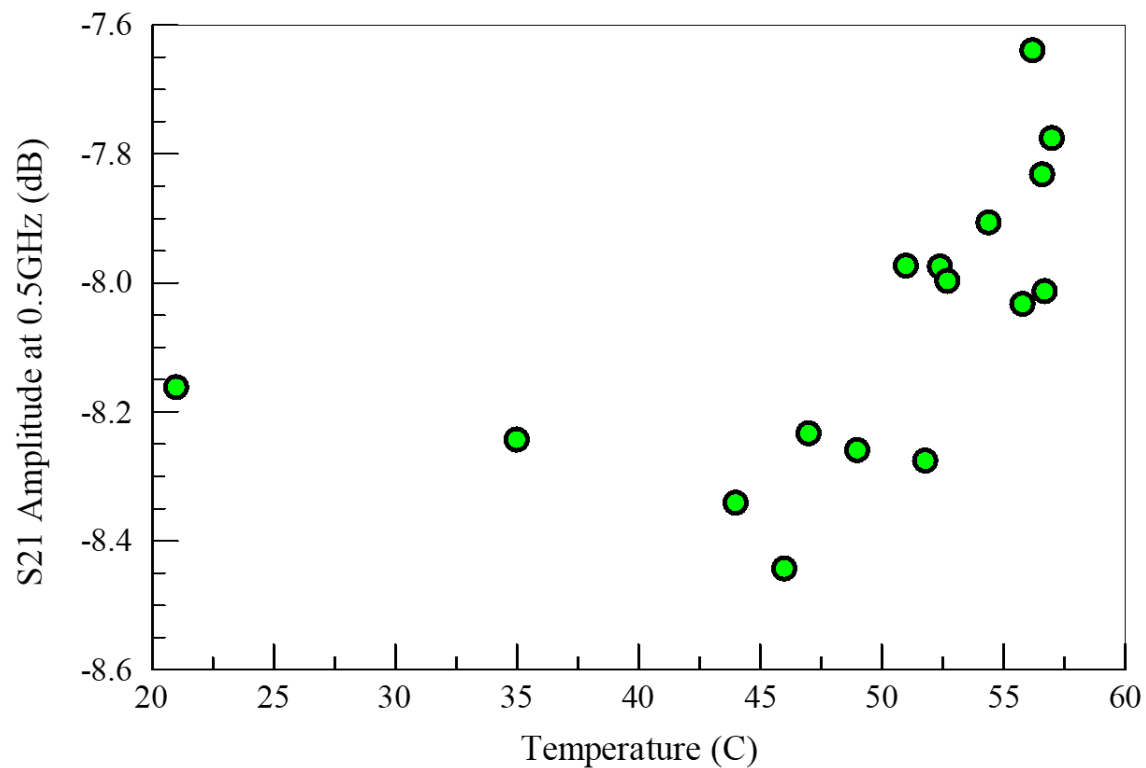


Figure 3: Impact of thermal anneal temperature on the electrical properties of $\text{Ge}_2\text{Sb}_2\text{Se}_5$ thin film that had been previously exposed to UV-AB radiation. The data represent both heating and cooling cycles. The data symbols are much larger than the one standard deviation error bars of the S_{21} measurements.

3.2 Surface Topography and Rheology

Figure 4 shows a comparison of the surface rheology of “as-received” to UV-modified surface. The photo-modified layer is about 10 nm deep and has a lower density and elastic modulus compared to the pristine surface. The elastic moduli of the “as-received” film and the photo-modified films were 140 and 88 MPa, respectively. The UV-modified surface is about 10 nm deep (i.e., involves the outermost ~1-2% of the film thickness). Amorphous chalcogenides are soft semiconductors due to the two-fold coordinated chalcogen atoms, which are susceptible to exhibit electro-atomic responses, and they behave as a flexible electron-lattice coupling system [38].

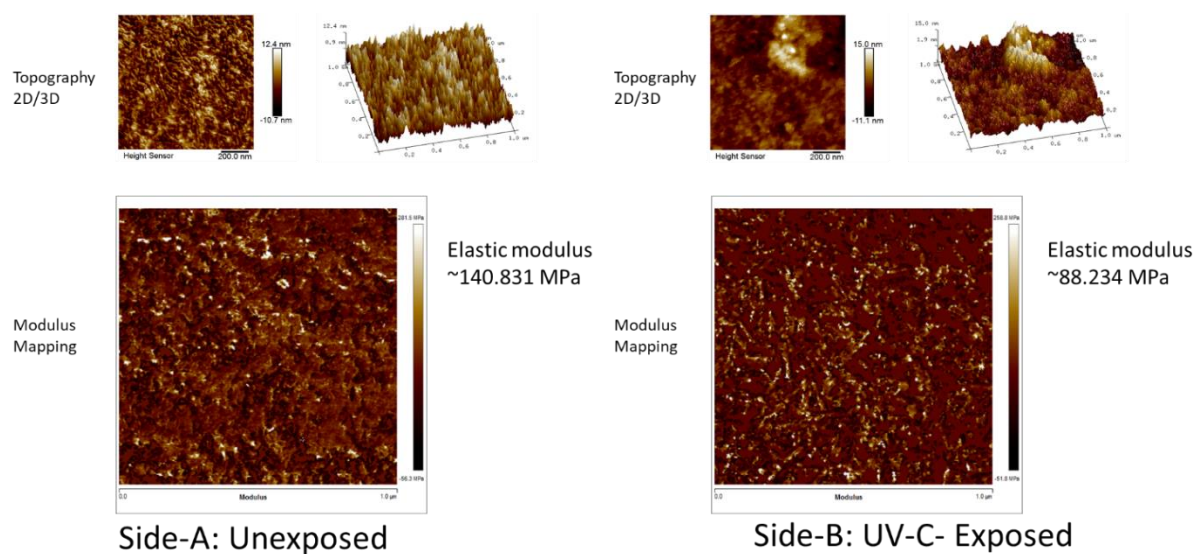


Figure 4: A comparison of the surface rheology of “As-Received” to UV-Modified Surface. The photo modified layer is about 10 nm deep and has lower density and elastic modulus compared to the pristine surface.

Figures 5 and 6 compare the impact of external stress on the surface morphology of a 820nm thick $\text{Ge}_2\text{Sb}_2\text{Se}_5$ thin film on Corning Pyrex glass measured with AFM. The data clearly shows applied stimuli induced topological changes. For example, UV exposure induces the formation of new surface features, increasing the surface RMS, while heating the film to temperatures around 60°C without photo exposure appears to smoothen the film’s surface (surface RMS falls below the RMS of the ‘as-received’ films). Furthermore, thermal annealing of the sample before UV-

This is the author's peer reviewed, accepted manuscript. However, the online version of record will be different from this version once it has been copyedited and typeset.
PLEASE CITE THIS ARTICLE AS DOI: 10.1063/1.50080142

irradiation did not prevent the formation of the low-density overlayer. Interestingly, these new features seem to disappear with subsequent heating to about 60°C.

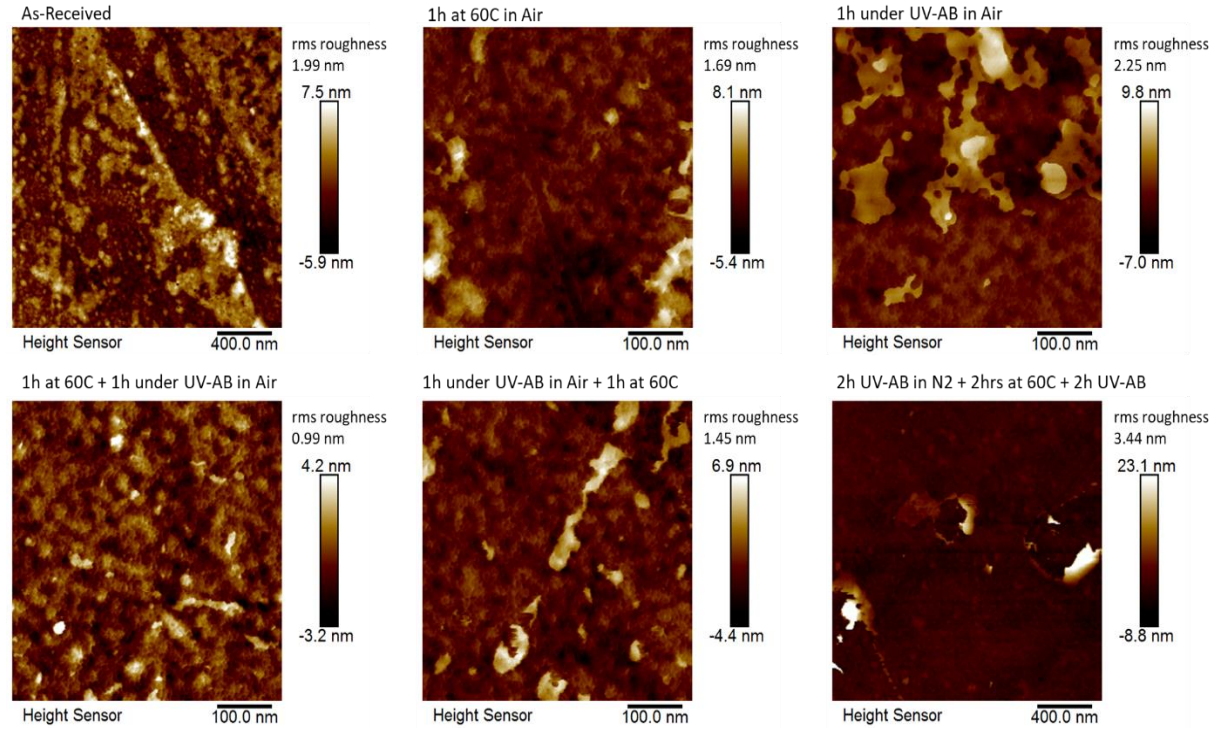


Figure 5: AFM comparison of the impact of UV exposure and annealing on the surface morphology of an 820 nm $\text{Ge}_2\text{Sb}_2\text{Se}_5$ thin film on Corning glass.

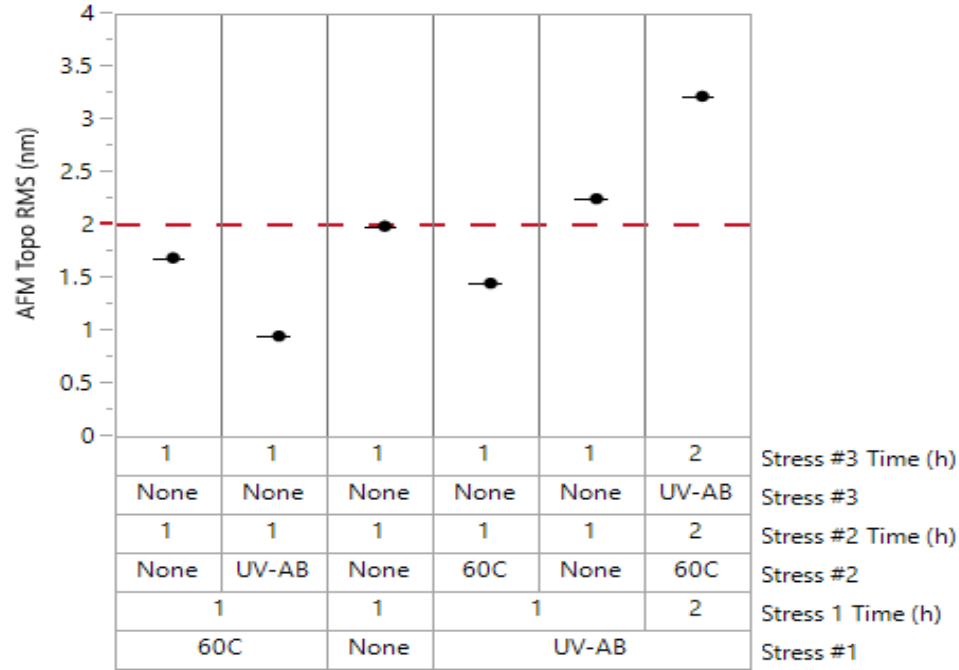


Figure 6: Comparison of the impact of external stimuli (heat at 60 °C, and UV-AB exposure, for 1h or 2h), on the $\text{Ge}_2\text{Sb}_2\text{Se}_5$ thin film / air interface roughness (surface RMS) measured by AFM.

3.3 Ellipsometric Evaluation of Photo-Induced Changes

Polarizability is related to many macro- and microscopic physical and chemical properties, such as optical UV absorption, ionic refraction, electro-optical effect, dielectric properties and ferroelectricity, and chemical stability along with optical nonlinearity. Specifically, optical nonlinearity is caused by electronic polarization of the material upon exposure to intense light beams, hence polarizability governs the optical response of materials [39].

Variable angle ellipsometry was used to characterize the photo-induced electrical changes described above. The spectroscopic ellipsometry (SE) optical data were used to determine the index of refraction (n) and the extinction coefficient (k) of the thin film materials as a function of photon energy E . In the analysis of SE data, all the unknown quantities were determined by minimizing the mean-squared error (MSE) function that contains *all* the experimental data from multiple angles of incidence and photon energy. We utilized an optical model consisting of a bulk amorphous thin film with an overlayer of photo-transformed material to determine the thickness and the optical properties (i.e., n and k), of the overlayer. The overlayer was assumed to be a physical mixture of the $\text{Ge}_2\text{Sb}_2\text{Se}_5$ bulk material and void (i.e., from the foamy appearance noted) and was modeled as an Effective Medium Approximation (EMA), which considers the material density. With these assumptions, the polarizability changes, as schematically illustrated in Figure 7.

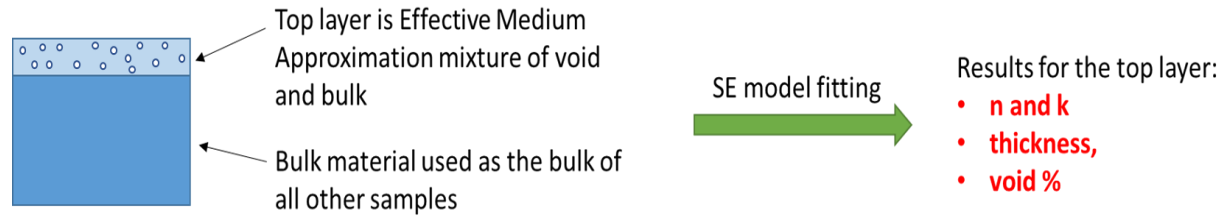


Fig 7: Schematic illustration of the Effective Medium Approximation (EMA) modeling strategy used on photo-exposed samples.

Fig. 8 compares the complex index of refraction obtained from SE data of the “as-received” and an un-irradiated sample heated to 60°C for one hour in N₂. The optical bandgap of the “as-received” sample was obtained from the Tauc-plot which is the function of $(\alpha E)^{1/2}$ vs. E where $\alpha = 4\pi k/\lambda$ is the absorption coefficient, and E and λ are the incident light photon energy and wavelength, respectively. The inset of Fig. 8 shows a linear fitting to the Tauc-plot in the vicinity of the bandgap resulting in the bandgap of 1.2 ± 0.1 eV[40]. It is obvious from the comparison that the heating does not significantly change the optical properties in the visible and UV spectral region since our prior results indicate that the crystallization onset of Ge₂Sb₂Se₅ is at approximately 300 °C [41]. On the other hand, as shown in Figure 9, the exposure of samples to UV light affects the complex index of refraction of the overlayer. Compared to the bulk “as-received” sample, the optical indices of the overlayer of UV treated samples are lower, implying that the material in the photo-transformed layer is less dense after the UV exposure, as illustrated by lower density after exposure to UV-C performed (see blue curve). Overall, the top layer thickness obtained from SE analysis falls in the range of about 1 nm even though the skin depth or penetration depth of UV light is estimated to be about 10 nm. Such shallow effects of UV exposure could be due to strong UV absorption by Ge₂Sb₂Se₅ resulting in less light intensity in the region below the surface.

This is the author's peer reviewed, accepted manuscript. However, the online version of record will be different from this version once it has been copyedited and typeset.
PLEASE CITE THIS ARTICLE AS DOI: 10.1063/1.50080142

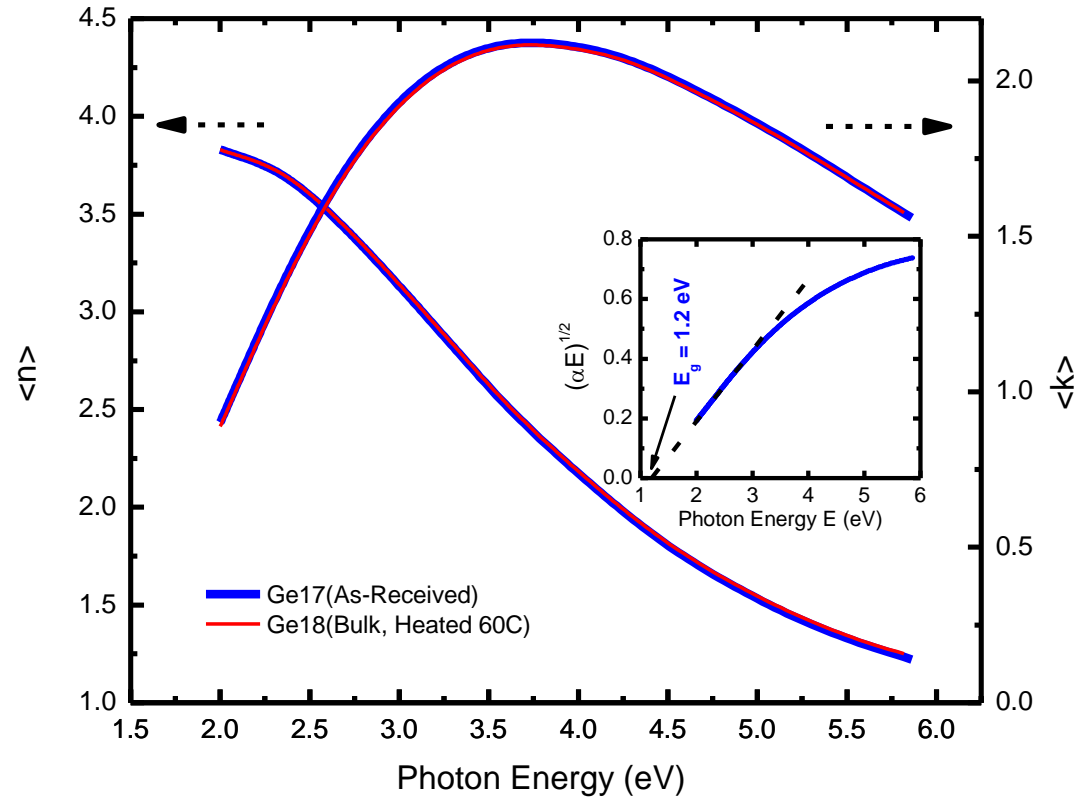


Figure 8: The complex index of refraction of the “as-received” sample, compared with that of the sample 18 (bulk, heated 60C). The inset is the Tauc-plot used to determine the optical band gap of the “as-received” sample.

This is the author's peer reviewed, accepted manuscript. However, the online version of record will be different from this version once it has been copyedited and typeset.
PLEASE CITE THIS ARTICLE AS DOI: 10.1063/1.50080142

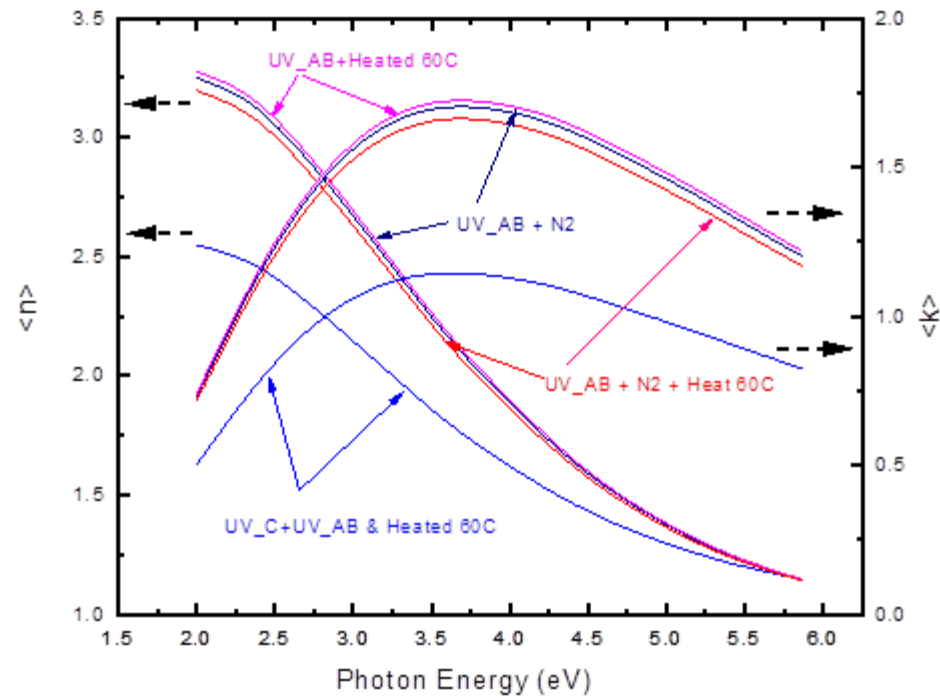


Figure 9: Comparison of changes in thin film optical constants as a function of applied stimuli, showing significant changes in the dielectric functions with UV-exposure.

To further understand the impact of external stimuli on the formation of the PIC overlayer, we varied experimental conditions by combining various stimuli, viz, heating, UV-AB wavelengths, UV-irradiation time. The thickness and composition of the photo-induced low-density secondary film were measured and modeled with variable angle spectroscopic ellipsometry (VASE). Figure 10 shows the impact of external stimuli on the composition (void fraction) of the secondary layer of the thin film / air interface. Figures 10A and 10B compare the impact of external stimuli on the calculated density and thickness respectively, of the overlayer at $\text{Ge}_2\text{Sb}_2\text{Se}_5$ thin film / air interface, measured by VASE. The red dashed line is the surface film void fraction of the 'as-received' film and added for reference only. Inspection of the figure shows that only UV-exposure induced voids in the film, and the void fraction increases with increasing exposure duration. From the changes in the optical constants, we conclude that only the UV-light exposure resulted in the formation of the overlayer, and heating to 60 °C for 1 hour in N_2 after photo-exposure seems to result in thinner overlayer thickness but does not totally revert the PIC layer to the original $\text{Ge}_2\text{Sb}_2\text{Se}_5$ material. Furthermore, the post-anneal residual layer appears to be of the same porosity as the overlayer formed by UB-AB irradiation and did not grow even after ten cycles. Thus, the thermal treatment did not result in a new film formation but induces a smoothing of

the chalcogenide film surface. This is consistent with the thermal accelerated relaxation of the film into an equilibrium state from the as-deposited amorphous film [42].

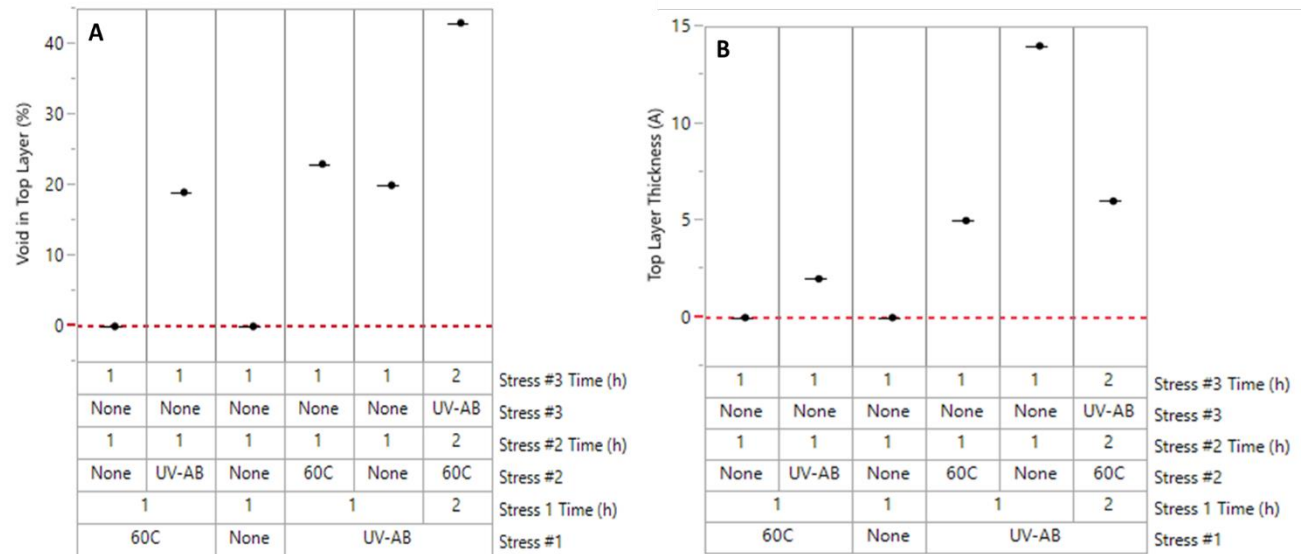


Figure 10: A and B compare the impact of external stimuli (heat at 60 °C, and UV-AB exposure, for 1h or 2h) on the calculated density and thickness, respectively, of the overlayer at Ge₂Sb₂Se₅ thin film / air interface. The red dashed line is the corresponding metric of the 'as-received' film and added for reference only.

The extinction coefficient, k , represents the material's ability for polarization. A comparison of Figures 6 and 7 shows that the extinction coefficient of the film decrease with UV-exposure, i.e., the film becomes more resistive possibly due to a decrease in carrier concentration and / or surface defect states and disorder [42]. This is also consistent with the increased insertion loss with photo exposure observed in Figures 3 and 4. Thus, the thermally induced reduction in insertion loss (Figure 5) suggests increased or partial regeneration of e-h pairs and surface defects, as the PIC layer does not totally revert to the original Ge₂Sb₂Se₅ material, as shown in Figure 10.

Electrically, the photo-formed overlayer at the film/air interface sets up a three-layer system: a physically intermediate composition layer, i.e., Boolchand phase [38], sandwiched between the isotropic bulk Ge₂Sb₂Se₅ layer and the photo-formed 'foamy' overlayer. [43]. This intermediate composition layer may represent a viable pathway for the recovery that leads to the partial reversibility of the PIC. The layer may have different polarizability from the cladding media and could make a significant contribution to the BDS transfer function of the MUT, i.e., $(h(f))$. This sandwich may be modeled electrically as an equivalent T-circuit.

4.0 Conclusions

UV-irradiation causes partially reversible photo-induced changes (PIC) in the outermost 2% of the 'as-deposited' bulk deposited film thickness to form a metastable layer at the air / thin film interface. The photo-formed layer is 'foamy' in morphology, with an elastic modulus of about 90 MPa compared to the 141 MPa for the bulk film, and is electrically more resistive than the bulk film. Modest heating, to about 60 °C, partially anneals out of the photo-formed foamy overlayer, to leave behind a very thin layer of thermally stable smooth material at the air/ bulk film interface. Re-exposure of the material to UV-light reforms the foamy layer, which anneals away with modest heating over several cycles. In summary, broadband dielectric spectroscopy provides further insights into the photo-induced processes in chalcogenide films. Specifically, we have observed reversible PIC-related electrical resistance changes in such films.

Acknowledgements

We thank former NIST summer student Andrew Obeng and Dr. Spencer Novak, now at Lightpath Technologies, Inc., for their work on other chalcogenide glass films that helped define the experimental parameters for the current work. M.Y.S. and J.H. acknowledges funding support from the MIT Skoltech Seed Fund Program

References

1. Naik, R., et al., *Laser-induced optical properties change in Sb₁₀S₄₀Se₅₀ chalcogenide thin films: An investigation through FTIR and XPS measurements*. Physica Status Solidi (B), 2014. **251**(3): p. 661-668.
2. Buisson, M., et al., *Mechanical model of giant photoexpansion in a chalcogenide glass and the role of photofluidity*. Physica B: Condensed Matter, 2017. **516**: p. 85-91.
3. Tikhomirov, V.K., et al., *Photoinduced volume changes related to photoinduced anisotropy in chalcogenide glasses*. Philosophical Magazine Letters, 2003. **83**(2): p. 117-124.
4. Sebastian, A., M. Le Gallo, and E. Eleftheriou, *Computational phase-change memory: beyond von Neumann computing*. Journal of Physics D: Applied Physics, 2019. **52**(44): p. 443002.
5. Bauers, S.R., et al., *Metal chalcogenides for neuromorphic computing: emerging materials and mechanisms*. Nanotechnology, 2021. **32**(37): p. 372001.
6. Feringa, B.L., et al., *Chiroptical Molecular Switches*. Chemical Reviews, 2000. **100**(5): p. 1789-1816.
7. Valev, V.K., et al., *Chirality and Chiroptical Effects in Plasmonic Nanostructures: Fundamentals, Recent Progress, and Outlook*. Advanced Materials, 2013. **25**(18): p. 2517-2534.
8. Borisenko, K.B., et al., *Photo-induced optical activity in phase-change memory materials*. Scientific Reports, 2015. **5**(1): p. 8770.

This is the author's peer reviewed, accepted manuscript. However, the online version of record will be different from this version once it has been copyedited and typeset.
PLEASE CITE THIS ARTICLE AS DOI: 10.1063/5.0080142

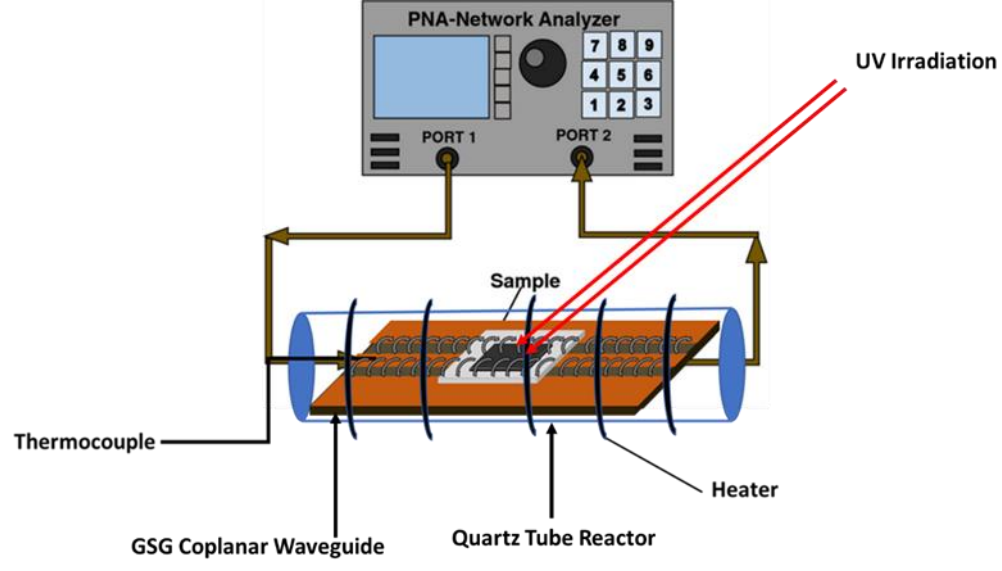
9. Musgraves, J.D., K. Richardson, and H. Jain, *Laser-induced structural modification, its mechanisms, and applications in glassy optical materials*. Optical Materials Express, 2011. **1**(5): p. 921-935.
10. Kolobov, A.V., P. Fons, and J. Tominaga, *Understanding Phase-Change Memory Alloys from a Chemical Perspective*. Scientific Reports, 2015. **5**(1): p. 13698.
11. Krecmer, P., et al., *Reversible Nanocontraction and Dilatation in a Solid Induced by Polarized Light*. Science, 1997. **277**(5333): p. 1799-1802.
12. Marghany, M., *Chapter 5 - Quantize of scattering theory*, in *Synthetic Aperture Radar Imaging Mechanism for Oil Spills*, M. Marghany, Editor. 2020, Gulf Professional Publishing. p. 73-92.
13. Quan, B., et al., *Dielectric polarization in electromagnetic wave absorption: Review and perspective*. Journal of Alloys and Compounds, 2017. **728**: p. 1065-1075.
14. Jaramillo, R. and J. Ravichandran, *In praise and in search of highly-polarizable semiconductors: Technological promise and discovery strategies*. APL Materials, 2019. **7**(10): p. 100902.
15. Rongzhen Chen, D.T.s.t.t.S.o.I.E.a.M., Department of Materials Science and Engineering, KTH Royal Institute of Technology, Sweden, , , *First-Principles Study on Electronic and Optical Properties of Copper-Based Chalcogenide Photovoltaic Materials*, in *School of Industrial Engineering and Management, Department of Materials, Science and Engineering*. 2017, KTH Royal Institute of Technology: Stockholm, Sweden.
16. Ambrosch-Draxl, C. and J.O. Sofo, *Linear optical properties of solids within the full-potential linearized augmented planewave method*. Computer Physics Communications, 2006. **175**(1): p. 1-14.
17. Schönhals, F.K.a.A., *Broadband Dielectric Spectroscopy*. 2003: Springer, Berlin, Heidelberg.
18. Entesari, K., R.E. Ghiri, and E. Kaya, *Broadband Dielectric Spectroscopy: Recent Developments in Microwave Time-Domain Techniques*. IEEE Microwave Magazine, 2021. **22**(6): p. 26-48.
19. Pozar, D.M., *Microwave engineering*. 2005, Hoboken, NJ: J. Wiley.
20. Kuwahara, Y. *Application of S parameter to the inverse scattering problem*. in *2017 11th European Conference on Antennas and Propagation (EUCAP)*. 2017.
21. Bartolotti, L.J., *The hydrodynamic formulation of time-dependent Kohn-Sham orbital density functional theory*. The Journal of Physical Chemistry, 1986. **90**(22): p. 5518-5523.
22. Amoah, P.K., et al., *Microwave Monitoring of Atmospheric Corrosion of Interconnects*. ECS Journal of Solid State Science and Technology, 2018. **7**(12): p. N143-N149.
23. Obrzut, J., *Surface conductance and microwave scattering in semicontinuous gold films*. Acta Imeko, 2015. **4**(3): p. 5.
24. Pozar, D.M., *Microwave engineering* 4th Edition ed. 2012, Hoboken, NJ: J. Wiley.
25. Petit, L., et al., *Compositional dependence of the nonlinear refractive index of new germanium-based chalcogenide glasses*. Journal of Solid State Chemistry, 2009. **182**(10): p. 2756-2761.
26. Hu, J., et al., *Fabrication and testing of planar chalcogenide waveguide integrated microfluidic sensor*. Optics Express, 2007. **15**(5): p. 2307-2314.
27. Pittenger, B., et al., *Nanoscale DMA with the Atomic Force Microscope: A New Method for Measuring Viscoelastic Properties of Nanostructured Polymer Materials*. JOM, 2019. **71**(10): p. 3390-3398.
28. Harland G. Tompkins, J.N.H., *Spectroscopic Ellipsometry: Practical Application to Thin Film Characterization*. 2016: Momentum Press.
29. Tikhomirov, V.K. and S.R. Elliott, *Model for photoinduced anisotropy and its dark relaxation in chalcogenide glasses*. Physical Review B, 1995. **51**(8): p. 5538-5541.
30. Zheng, Y., *Athermal Activation in Glassy Fluid*. 2021.
31. Kastner, M., D. Adler, and H. Fritzsche, *Valence-Alternation Model for Localized Gap States in Lone-Pair Semiconductors*. Physical Review Letters, 1976. **37**(22): p. 1504-1507.

This is the author's peer reviewed, accepted manuscript. However, the online version of record will be different from this version once it has been copyedited and typeset.
PLEASE CITE THIS ARTICLE AS DOI: 10.1063/5.0080142

32. Ahmed, I., et al., *There is plenty of room at the top: generation of hot charge carriers and their applications in perovskite and other semiconductor-based optoelectronic devices*. Light: Science & Applications, 2021. **10**(1): p. 174.
 33. Rodriguez, J.R., et al., *Ge₂Sb₂Se₅ Glass as High-capacity Promising Lithium-ion Battery Anode*. Nano Energy, 2020. **68**: p. 104326.
 34. Banik, I., et al., *Some open problems in physics of disordered materials (and their possible solutions on the base of the barrier-cluster-heating model)*. AIP Conference Proceedings, 2013. **1564**(1): p. 117-122.
 35. Malinovsky, V.K. and N.V. Surovtsev, *Optical Memory in Chalcogenide Glasses*. Chalcogenide Letters, 2012. **9**(2): p. 79-84.
 36. Gütlich, P., A. Hauser, and H. Spiering, *Thermal and Optical Switching of Iron(II) Complexes*. Angewandte Chemie International Edition in English, 1994. **33**(20): p. 2024-2054.
 37. Amoah, P.K., et al., *Broadband Dielectric Spectroscopic Detection of Volatile Organic Compounds with ZnO Nanorod Gas Sensors*. Journal of Physics D: Applied Physics, 2020.
 38. Popescu, M., *Disordered chalcogenide optoelectronic materials: Phenomena and applications*. Journal of Optoelectronics and Advanced Materials, 2005. **7**(4): p. 2189-2210.
 39. Shannon, R.D., *Dielectric polarizabilities of ions in oxides and fluorides*. Journal of Applied Physics, 1993. **73**(1): p. 348-366.
 40. Tauc, J., *Optical Properties of Amorphous Semiconductors*, in *Amorphous and Liquid Semiconductors*, J. Tauc, Editor. 1974, Springer US: Boston, MA. p. 159-220.
 41. Zhang, Y., et al., *Broadband transparent optical phase change materials for high-performance nonvolatile photonics*. Nature Communications, 2019. **10**(1): p. 4279.
 42. Sahoo, D., et al., *Role of annealing temperature on optimizing the linear and nonlinear optical properties of As₄₀Se₅₀Ge₁₀ films*. RSC Advances, 2020. **10**(45): p. 26675-26685.
 43. Glybovski, S.B., et al., *Metasurfaces: From microwaves to visible*. Physics Reports, 2016. **634**: p. 1-72.
-

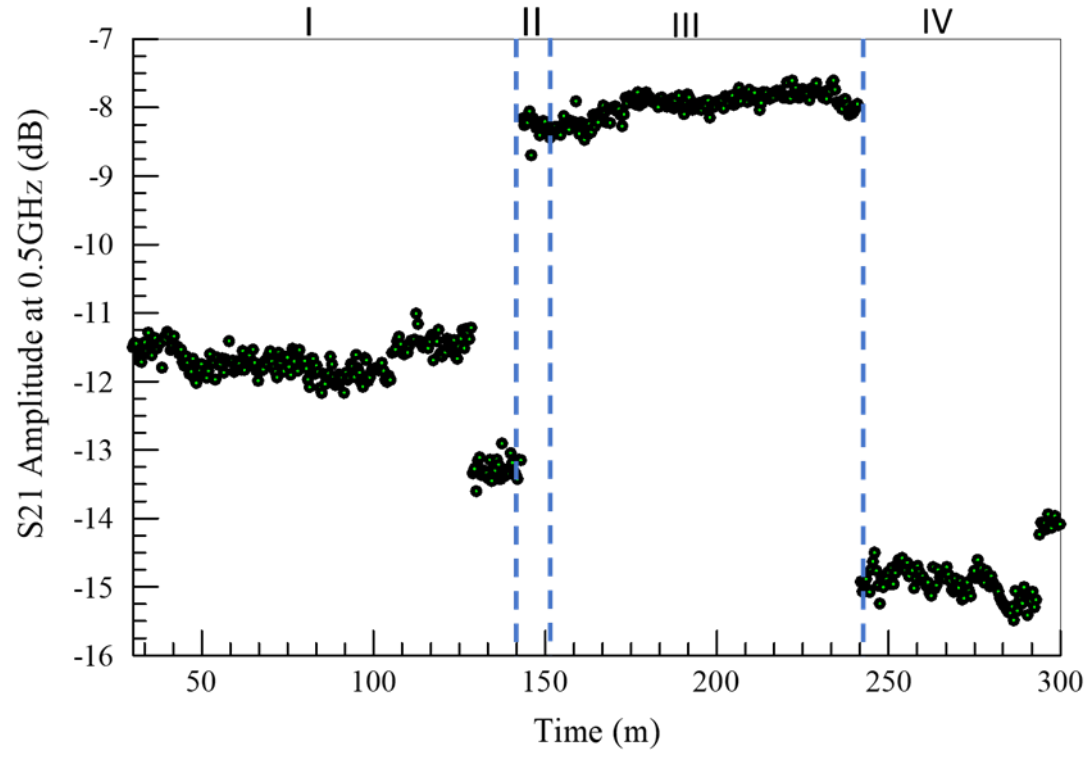
This is the author's peer reviewed, accepted manuscript. However, the online version of record will be different from this version once it has been copyedited and typeset.

PLEASE CITE THIS ARTICLE AS DOI: 10.1063/5.0080142

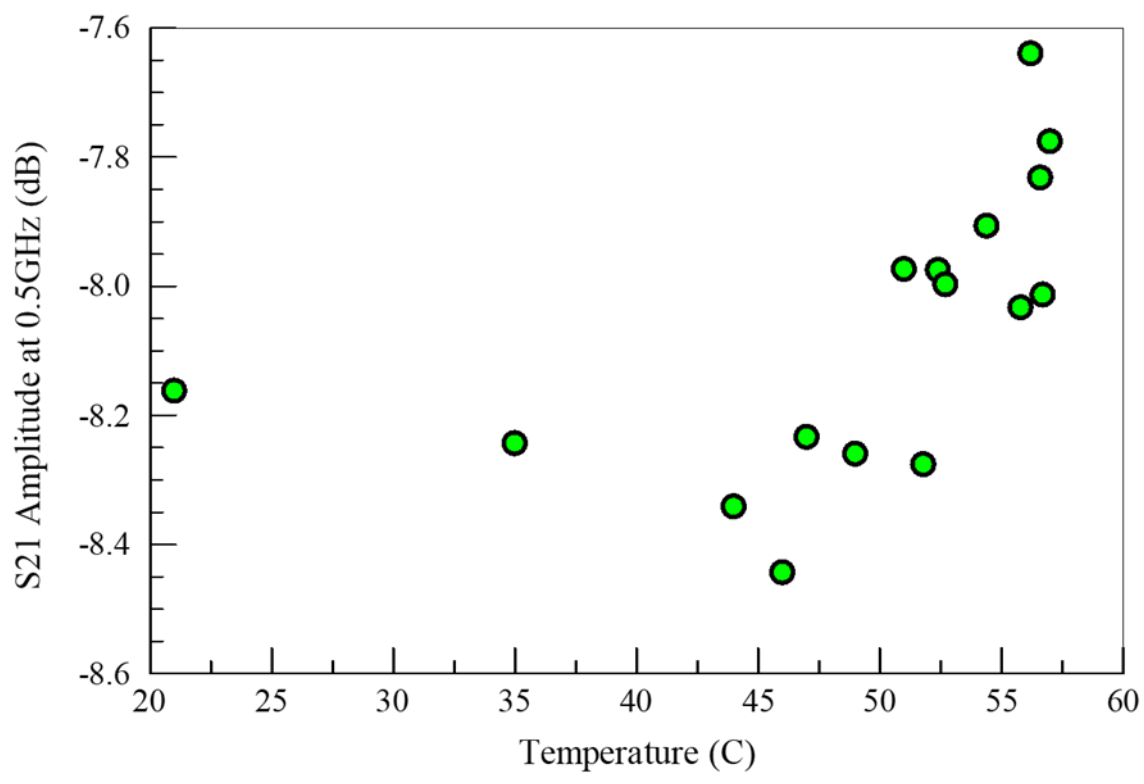


This is the author's peer reviewed, accepted manuscript. However, the online version of record will be different from this version once it has been copyedited and typeset.

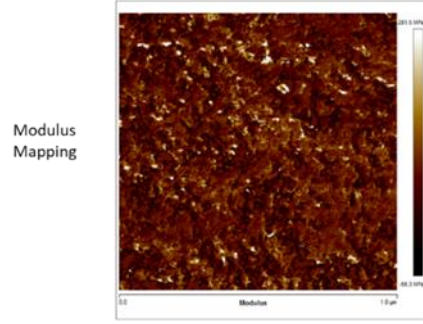
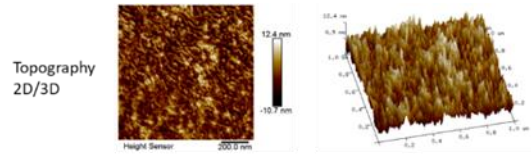
PLEASE CITE THIS ARTICLE AS DOI: 10.1063/5.0080142



This is the author's peer reviewed, accepted manuscript. However, the online version of record will be different from this version once it has been copyedited and typeset.
PLEASE CITE THIS ARTICLE AS DOI: 10.1063/5.0080142

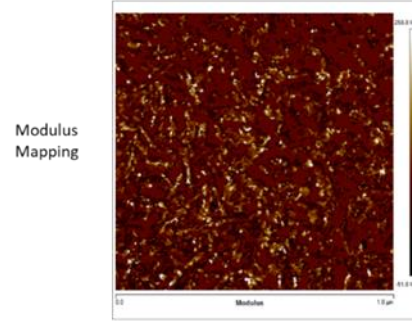
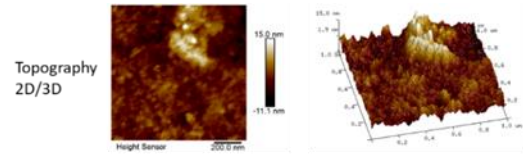


This is the author's peer reviewed, accepted manuscript. However, the online version of record will be different from this version once it has been copyedited and typeset.
PLEASE CITE THIS ARTICLE AS DOI: 10.1063/5.0080142



Elastic modulus
~140.831 MPa

Side-A: Unexposed

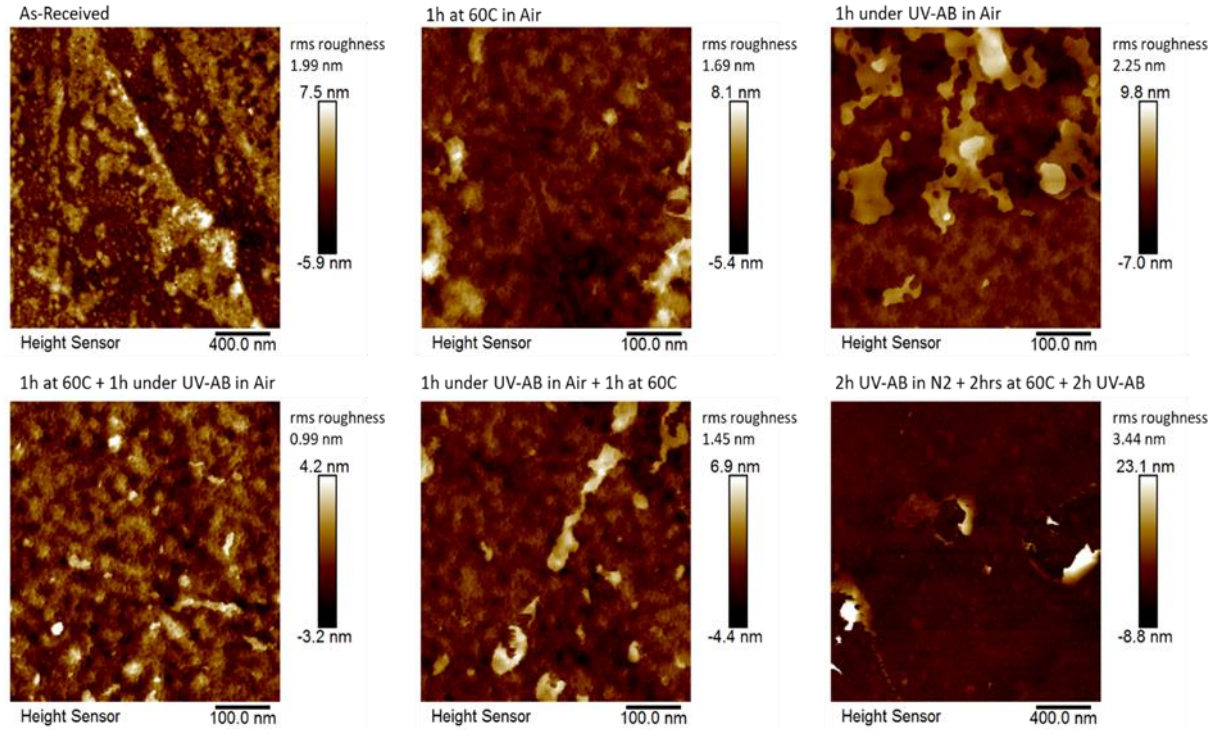


Elastic modulus
~88.234 MPa

Side-B: UV-C- Exposed

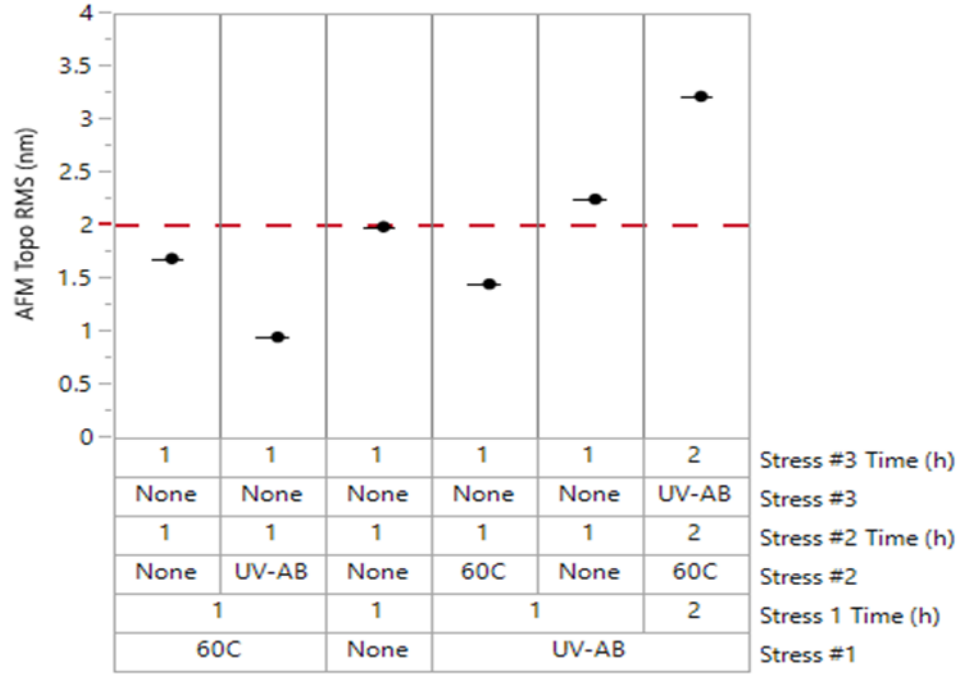
This is the author's peer reviewed, accepted manuscript. However, the online version of record will be different from this version once it has been copyedited and typeset.

PLEASE CITE THIS ARTICLE AS DOI: 10.1063/1.50080142



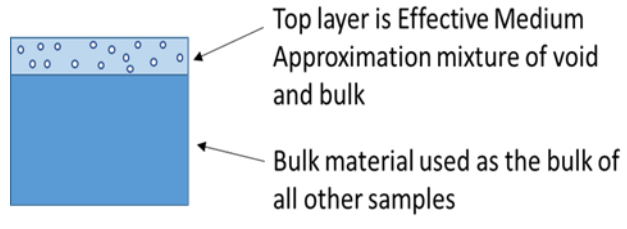
This is the author's peer reviewed, accepted manuscript. However, the online version of record will be different from this version once it has been copyedited and typeset.

PLEASE CITE THIS ARTICLE AS DOI: 10.1063/5.0080142

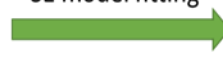


This is the author's peer reviewed, accepted manuscript. However, the online version of record will be different from this version once it has been copyedited and typeset.

PLEASE CITE THIS ARTICLE AS DOI: 10.1063/5.0080142



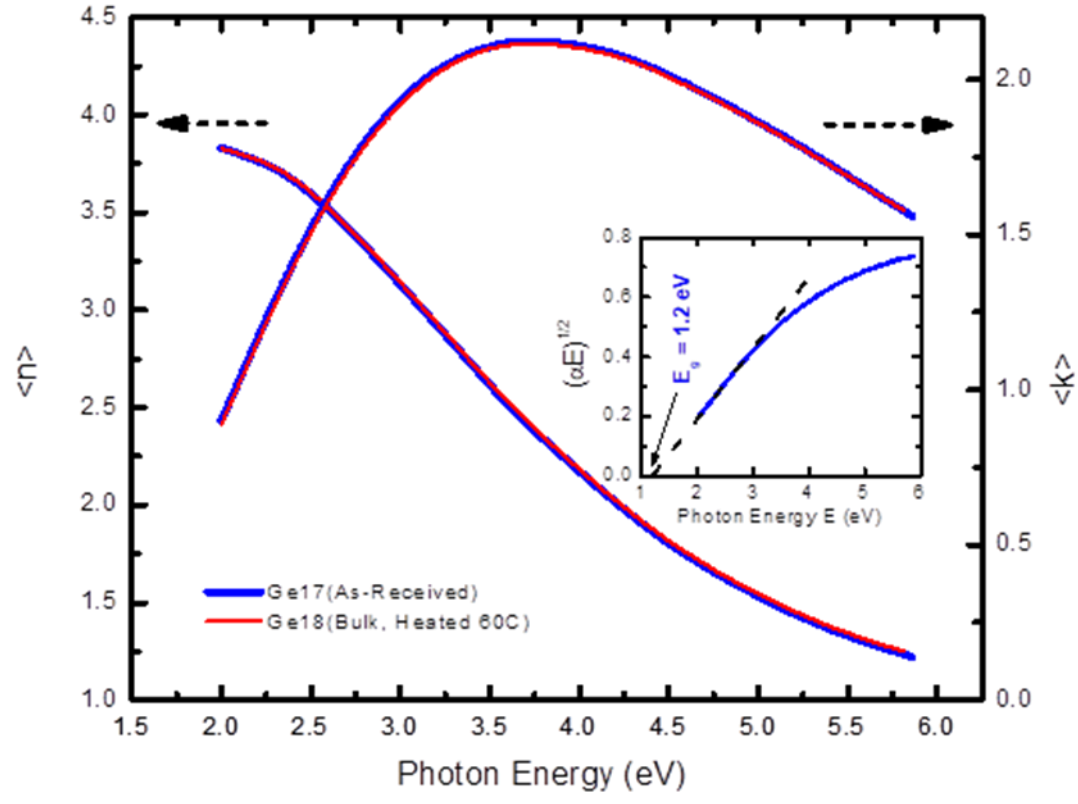
SE model fitting



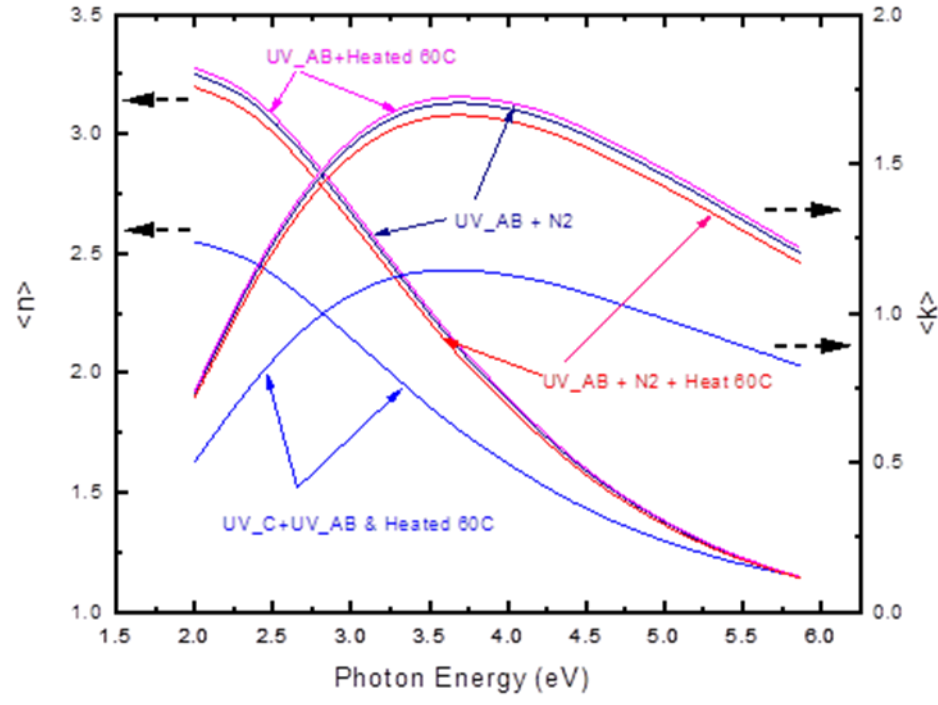
Results for the top layer:

- **n and k**
- **thickness,**
- **void %**

This is the author's peer reviewed, accepted manuscript. However, the online version of record will be different from this version once it has been copyedited and typeset.
PLEASE CITE THIS ARTICLE AS DOI: 10.1063/5.0080142



This is the author's peer reviewed, accepted manuscript. However, the online version of record will be different from this version once it has been copyedited and typeset.
PLEASE CITE THIS ARTICLE AS DOI: 10.1063/5.0080142



This is the author's peer reviewed, accepted manuscript. However, the online version of record will be different from this version once it has been copyedited and typeset.
PLEASE CITE THIS ARTICLE AS DOI: 10.1063/5.0080142

